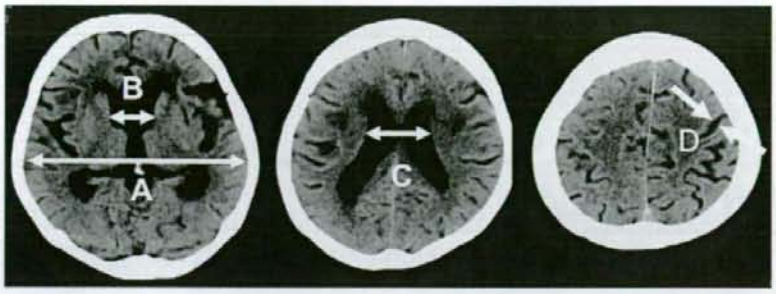

Fig. 1. Methods for calculation of cerebrospinal fluid–cranial ratio (CCR): (A) maximal distance between the internal tables of the skull, (B) minimal width of the frontal horns, (C) minimal width of bodies of the lateral ventricles, and (D) number of sulci of 3.3 mm or greater on a slice 7 cm above the orbitomeatal line. CCR is obtained by $42.66 \times B/A + 12.52 \times C/A + 0.232 \times D - 2.92$.

properly evaluate the incidence of radiation-induced brain atrophy and dementia, we considered it necessary to carry out a prospective study to exclude as much as possible the influence of other factors. In this report, we present results of a prospective study of the Chubu Radiation Oncology Group, Japan (CROG-0301), that estimated the incidence of decrease in Mini-Mental State Examination (MMSE) scores (14) and brain atrophy after WBRT in patients with brain metastases who did not undergo a neurosurgical operation or concurrent chemotherapy.

METHODS AND MATERIALS

Eligibility

Patients who met the following criteria were considered for entry: those who were judged to be indicated for treatment with WBRT alone, with no prior brain surgery, with an MMSE score of at least 21, those who were not using and would not use corticosteroids for longer than 2 weeks, and those expected to survive at least 3 months. Considering the possibility that the presence of tumors may lower the MMSE score before treatment, the lower limit of MMSE score was set at 21, but all except 1 patient had an MMSE score of 23 or higher. This study was approved by the respective institutional review boards. Informed consent was obtained from all patients.

Table 1. Characteristics of 101 patients who entered the study

Age (y)	62 (31–78)
Men/women	52/49
WHO performance status (0/1/2/3)	9/28/33/31
Primary tumor (lung/breast/bone/colon/other)	67/24/3/2/5
Tumor number (1/2/3/≥4)	7/10/15/69
Largest tumor diameter (cm)	2.0 (0.6–8.0)
MMSE score	28 (21–30)
Cerebrospinal fluid–cranial ratio	5.5 (1.5–9.8)
Imaging modality (MRI/CT)	67/34
Total radiation dose (50/40/<40 Gy)	66/26/9
No. of assessable patients at 0/3/6/9/12/15/18/24/30/36 mo	92/68/45/30/25/17/10/4/3/3

Abbreviations: WHO = World Health Organization; MMSE = Mini-Mental State Examination; MRI = magnetic resonance imaging; CT = computed tomography.

Values expressed as median (range) or number.

We intended to obtain at least 40 assessable patients at 6 months to determine the incidence of brain atrophy and MMSE score decrease with a 95% confidence interval (CI) ± 15%. Because median survival time of patients with brain metastases was usually 4–6 months (15), but patients with an expected survival time less than 3 months were excluded from entry, it was considered necessary to accrue 100 patients.

Treatment

After evaluation, patients underwent WBRT with 2-Gy daily fractions up to 40 Gy over 4 weeks by using parallel-opposing fields. The dose was prescribed at the midline. Thereafter, a boost to main tumor sites was given when possible, with 10 Gy in five fractions. Even in patients with multiple metastases, booster radiation was recommended by excluding as much normal brain tissues as possible. When radiation field reduction was considered difficult, radiotherapy was stopped at 40 Gy. Chemotherapy was prohibited until 2 weeks after completion of WBRT.

Evaluation

Before WBRT, patients underwent contrast-enhanced magnetic resonance imaging (MRI) and/or computed tomography (CT) of the brain, in addition to physical examination and MMSE. These examinations were repeated immediately after WBRT, every 3 months for 18 months, and every 6 months thereafter. For follow-up, use of the same imaging modality (*i.e.*, either MRI or CT) was mandatory. Brain atrophy was evaluated as change in cerebrospinal fluid–cranial ratio (CCR), as proposed by Nagata *et al.* (16); the method is shown in Fig. 1. Briefly, the CCR was calculated from the equation shown in the caption of Fig. 1 by measuring the maximal distance between the internal tables of the skull, minimum width of the frontal horns of the bilateral lateral ventricles, minimum width of the bodies of the bilateral lateral ventricles, and the number of widened sulci (≥3.3 mm) on a slice 7 cm above the orbitomeatal line. The atrophy index was defined as postradiation CCR divided by preradiation CCR. Differences in incidences of brain atrophy and MMSE score decrease between groups were examined by means of Fisher's exact test. The MMSE was performed by the same radiation oncologists for respective patients.

Evaluation was terminated when intracranial lesions progressed so that evaluation was considered to be influenced by disease progression or second-line treatment became necessary. Data for these patients before this point of intracranial progression were used for analysis.

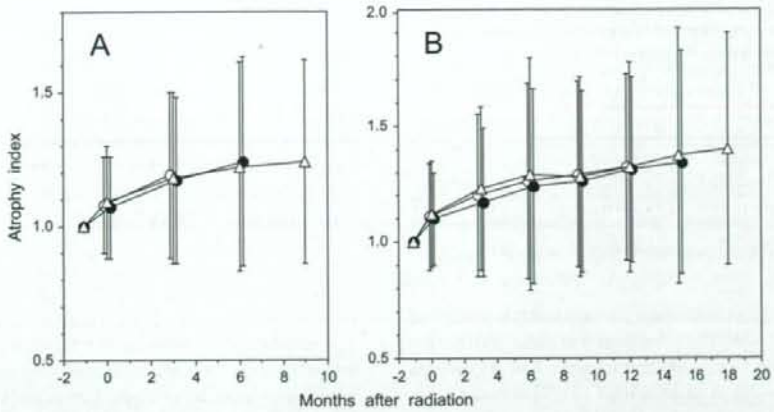

Fig. 2. Changes in mean atrophy index (A) in 68, 45, and 30 patients who were assessable for 3 (open circle), 6 (closed circle), and 9 months (open square); and (B) 25, 17, and 10 patients assessable for 12 (open circle), 15 (closed circle), and 18 months (open square), respectively. Bars represent SD.

RESULTS

Between Jan 2002 and Aug 2006, a total of 115 patients were evaluated for entry, but 14 were excluded because of low MMSE scores. Table 1 lists characteristics of the 101 patients who entered the study. Median patient age was 62 years. Ninety-three percent of patients had multiple tumors. Nine patients could not complete the planned radiotherapy because of deterioration in general conditions in 8 patients and change in treatment policy in 1 patient; therefore, post-treatment evaluation was not possible. Of the remaining 92 patients, 66 received a total dose of 50 Gy, whereas 26 underwent WBRT with 40 Gy alone.

Figure 2 shows changes in atrophy index values in groups of patients who were assessable for 3–18 months. The atrophy index tended to increase over time, although SDs were relatively large. The trend toward a mild increase in the atrophy index at completion of radiotherapy was considered to be caused by tumor response; therefore, brain atrophy was evaluated by regarding the atrophy index at completion of radiotherapy as the control level in each patient. Compared with the index at completion of radiotherapy, atrophy increased by 30% or more in 9 of 68 patients (13%; 95% CI, 5.0–21) who were assessable at 3 months, 8 of 45 patients (18%; 95% CI, 6.8–29) at 6 months, 5 of 30 patients (16%; 95% CI, 2.9–29) at 9 months, 7 of 25 patients (28%; 95% CI, 10–46) at 12 months, 5 of 17 patients (29%; 95% CI, 7.4–51) at 15 months, 3 of 10 patients (30%; 95% CI, 1.6–58) at 18 months, and 3 of 4 patients (75%; 95% CI, 33–100) at 24 months. Of 3 patients who were assessable at both 30 and 36 months, increases in atrophy index by 30% or more were seen in 2 (67%; 95% CI, 14–100). Tables 2 and 3 list incidences of 30% or greater increase in atrophy index compared with the index value immediately after radiotherapy according to patient age and radiation dose, respectively. There were no apparent differences in incidence according to age and radiation dose, although patients receiving 50 Gy (40-Gy WBRT + 10-Gy boost) tended to have a greater incidence at 9 and 12 months. Table 4 lists the incidence of 30% or greater increase in atrophy index according to pretreatment CCR. At 12 and 15 months, the incidence was greater in patients with a pretreatment CCR less than median than in those with a CCR at or greater than median.

Figure 3 shows changes in MMSE scores in groups of patients who were assessable for 3 to 18 months. Mean MMSE scores were relatively constant, and no apparent decreases were observed. However, individually, decreases in MMSE scores of four points or more were observed in 5 of 68 patients

Table 2. Incidence of 30% or greater increases in atrophy index compared with immediately after whole-brain radiation according to patient age

	Months after whole-brain radiation					
Age (y)	3	6	9	12	15	18
<60	2/32	6/27	3/16	5/13	4/9	3/5
≥60	7/36	2/18	2/14	2/12	1/8	0/5
p	0.16	0.45	1.0	0.38	0.29	0.17
<70	8/54	8/38	5/25	7/22	5/15	3/9
≥70	1/14	0/7	0/5	0/3	0/2	0/1
p	0.67	0.32	0.56	0.53	0.56	1.0

Table 3. Incidence of 30% or greater increase in atrophy index compared with immediately after whole-brain radiation according to radiation dose

	Months after whole-brain radiation					
Dose (Gy)	3	6	9	12	15	18
40 (without boost)	3/19	2/13	0/6	0/4	0/1	—
50 (with boost)	6/49	6/32	5/24	7/21	5/16	3/4
p	1.0	1.0	0.55	0.29	1.0	—

Table 4. Incidence of 30% or greater increases in atrophy index compared with immediately after whole-brain radiation according to pretreatment CCR

	Months after whole-brain radiation					
CCR	3	6	9	12	15	18
<Median	6/34	6/22	4/15	7/12	5/8	3/5
≥Median	3/34	2/23	1/15	0/13	0/9	0/5
p	0.48	0.13	0.33	0.0052	0.029	0.17

Abbreviation: CCR = cerebrospinal fluid–cranial ratio.

(7.4%; 95% CI, 1.2–14) who were assessable at 3 months, 5 of 45 patients (11%; 95% CI, 1.9–20) at 6 months, 6 of 30 patients (20%; 95% CI, 5.7–34) at 9 months, 3 of 25 patients (12%; 95% CI, 0–25) at 12 months, 1 of 17 patients (5.9%; 95% CI, 0 – 17) at 15 months, 0 of 10 patients (0%) at 18 months, 0 of 4 patients (0%) at 24 months, and 0 of 3 patients at 30 and 36 months. Table 5 lists incidences of MMSE score decrease according to patient age; there were no significant differences in incidence according to age. About half the patients with an MMSE score decrease had systemic disease progression (outside the central nervous system). There appeared to be no correlation between brain atrophy and MMSE decrease (data not shown). Seven patients received systemic chemotherapy during follow-up periods, and 1 patient had a decrease in MMSE score of four points or more at 6–12 months.

DISCUSSION

The apprehension that WBRT might cause brain atrophy and dementia seems to have grown gradually among medical oncologists and neurosurgeons. Several retrospective studies suggested it (6–11), but others reported maintenance of neurocognitive function in long-term survivors with glioma and other primary brain tumors after radiation therapy (17–20). Because retrospective studies cannot exclude the influence of other factors, such as surgery, chemotherapy, and disease progression, that can be associated with the development of brain atrophy and dementia, we conducted the present prospective study and attempted to eliminate as many of these factors as possible. As a result, we found that brain atrophy can develop in a proportion of patients, but decrease in MMSE scores was relatively infrequent. It was reported that other radiologic findings can develop after radiation to the brain, especially on MRI (21), but we used brain atrophy as an end point because it often is regarded as a late sequela of radiation linked to dementia (9). Another reason is that MRI was difficult to perform because of the long waiting time for booking in some institutions; however, brain atrophy could be evaluated easily by using CT.

We used the method of Nagata *et al.* (16) to evaluate brain atrophy. It is a simple method that can be used in multi-institutional studies, but the widths of the lateral ventricles and sulci are influenced by the mass effect of the tumors. An increase in atrophy index was found in many patients at completion of radiation therapy. This was not caused by brain atrophy, but rather tumor shrinkage. Therefore, we used atrophy index at the completion of radiotherapy as a control to evaluate posttreatment brain atrophy in individual patients. Asai *et al.* (9) reported the development of brain atrophy in 56% of patients undergoing radiation therapy. They used Nagata's method, as we did, but they defined development of brain atrophy as an atrophy index of 1.13 or higher. In our experience, measurement of CCR is not accurate enough to ensure that an atrophy index of 1.13 really represents brain atrophy. We believe an atrophy index of 1.3 is reasonable for visual recognition of brain atrophy on MRI and CT. In addition, all patients in the study of Asai *et al.* (9) had

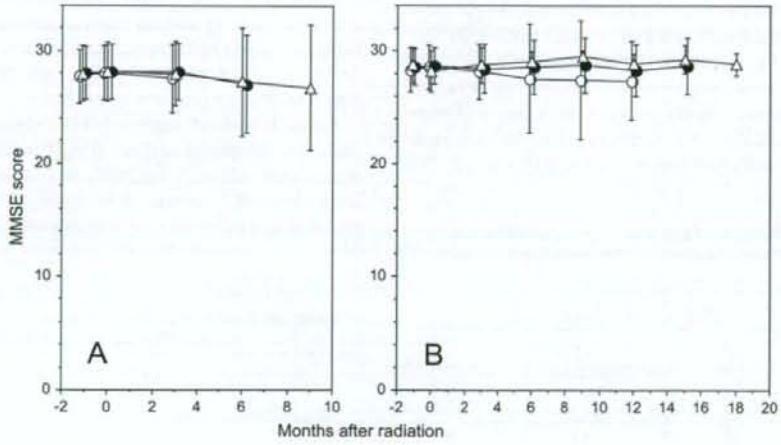

Fig. 3. Changes in mean Mini-Mental State Examination (MMSE) scores in (A) 68, 45, and 30 patients who were assessable for 3 (open circle), 6 (closed circle), and 9 months (open triangle); and (B) 25, 17, and 10 patients assessable for 12 (open circle), 15 (closed circle), and 18 months (open square), respectively. Bars represent SD.

Table 5. Incidence of decrease in Mini-Mental State Examination score of four or more points after whole-brain radiation according to patient age

	Months after whole-brain radiation					
Age (y)	3	6	9	12	15	18
<60	1/32	1/27	1/16	1/13	0/9	0/5
≥60	4/36	4/18	5/14	2/12	1/8	0/5
p	0.36	0.14	0.072	0.59	1.0	—
<70	4/54	4/38	4/25	3/22	1/15	0/9
≥70	1/14	1/7	2/5	0/3	0/2	0/1
p	1.0	1.0	0.55	1.0	1.0	—

undergone brain surgery. They reported that no brain atrophy was found after brain surgery alone, but it is not known whether surgery can be an additive factor in the development of brain atrophy when combined with radiation. In our study, excluding the influence of brain surgery, we found brain atrophy in up to 30% of patients at 6–18 months. However, about 40–50% of patients maintained an atrophy index of around 1 during these periods. We could not prove an association between the incidence of atrophy and patient age or use of the 10-Gy boost. Meanwhile, patients with a pretreatment CCR less than the median value had a greater incidence of increase in the atrophy index. This is in contrast to findings reported by Nieder *et al.* (22) showing that patients with preexisting atrophy had a greater risk of continuous deterioration. One reason for the finding in the present study may be that the index is likely to increase when the denominator (pretreatment CCR) is small.

The MMSE alone is considered to be an insensitive method to evaluate higher brain dysfunction, and it now seems clear that the combination of various neurologic tests is necessary to evaluate more subtle cognitive dysfunction (23). Therefore, the aim of the present study is to detect apparent dementia. In a prospective study comparing WBRT plus SRS and SRS alone, Aoyama *et al.* (24) evaluated changes in MMSE scores in a proportion of patients. They found that although there was no significant difference in change in MMSE scores after treatment between the two groups, the scores tended to decrease, especially after WBRT plus SRS. However, they did not clearly differentiate between disease progression–induced deterioration and treatment-related decrease. In the present study, mean MMSE score did not decrease on the whole, and proportions of patients with an MMSE score decrease of four points or more were only 11% at 6 months, 12% at 1 year, and 0% at 18 months. We excluded patients with intracranial progressive disease from further evaluation, but we did not exclude patients with systemic disease progression. As a consequence, about half the patients with an MMSE score decrease had systemic progressive disease and a decrease in performance status; thus, purely radiation-induced decrease appeared to be still less frequent. In the present study, only brain atrophy was evaluated by using MRI and CT, and there appeared to be no correlation between brain atrophy and MMSE score decrease. In additional investigations, we plan to evaluate MRI findings that may characterize patients with an MMSE score decrease.

Radiation dose per fraction may influence the occurrence of late morbidity for radiation therapy. It is well-known that central nervous system tissues have low α/β ratios and therefore are susceptible to greater doses per fraction (25). In WBRT for brain metastases, 10 fractions of 3 Gy commonly are used, but we did not use the 3-Gy/d dose in this study in the belief that a 2-Gy/d fraction is better than a 3-Gy fraction in terms of preventing late adverse effects in long-term survivors. Most previous studies reporting deterioration in neurocognitive function used 3-Gy or even higher doses per fraction (6–8, 26). In addition, 10 fractions of 3 Gy given for prophylactic cranial irradiation in patients with small-cell lung cancer are considered to be more likely to produce neurotoxicity than 2- or 2.5-Gy/d fractions (26–29). In a Radiation Therapy Oncology Group study using 10 fractions of 3 Gy for brain metastases, 81%, 66%, and 57% of patients maintained an MMSE score higher than 23 at 6, 12, and 18 months, respectively (30). Although the biologically effective dose for 10 fractions of 3 Gy is less than that for 20 fractions of 2 Gy assuming an α/β ratio of 1–4 Gy, the incidence appeared greater than that observed in the present study. Thus, use of a 2-Gy/d fraction might have contributed to the favorable effects on neurocognitive function observed in the present study. Of course, we use 3-Gy fractions for palliative cases and patients with a short expected survival time, but we will continue to use the 2-Gy fraction for patients expected to survive longer than 6 months.

In summary, the present study shows that brain atrophy can develop after WBRT in a certain proportion of patients (up to 30%), but a decrease in MMSE scores was less frequent. Avoiding WBRT for the reason that it causes dementia appears to be a groundless idea in patients with metastatic brain tumors. The WBRT with or without stereotactic boosts should be a reasonable treatment for patients with multiple brain metastases.

REFERENCES

1. Khuntia D, Brown P, Li J, *et al.* Whole-brain radiotherapy in the management of brain metastasis. *J Clin Oncol* 2006;24:1295–1304.
2. Sneed PK, Lamborn KR, Forstner J, *et al.* Radiosurgery for brain metastases: Is whole brain radiotherapy necessary? *Int J Radiat Oncol Biol Phys* 1999;43:549–558.
3. Serizawa T, Higuchi Y, Ono J, *et al.* Gamma knife surgery for metastatic brain tumors without prophylactic whole-brain radiotherapy: Results in 1000 consecutive cases. *J Neurosurg* 2006;105(Suppl.):S86–S90.
4. Yamamoto M, Ide M, Nishio S, *et al.* Gamma knife radiosurgery for numerous brain metastases: Is this a safe treatment? *Int J Radiat Oncol Biol Phys* 2002;53:1279–1283.
5. Amendola BE, Wolf A, Coy S, *et al.* Radiosurgery as palliation for brain metastases: A retrospective review of 72 patients

harboring multiple lesions at presentation. *J Neurosurg* 2002; 97(Suppl.):S511–S514.
6. Hindo WA, DeTrana FA, Lee MS, *et al.* Large dose increment irradiation in treatment of cerebral metastasis. *Cancer* 1970;26: 138–141.
7. Young DF, Posner JB, Chu F, *et al.* Rapid-course radiation therapy of cerebral metastasis: Results and complications. *Cancer* 1974;34:1069–1076.
8. DeAngelis LM, Delattre JY, Posner JB. Radiation-induced dementia in patients cured of brain metastases. *Neurology* 1989; 39:789–796.
9. Asai A, Matsutani M, Kohno T, *et al.* Subacute brain atrophy after radiation therapy for malignant brain tumor. *Cancer* 1989;63:1962–1974.
10. Ueki K, Matsutani M, Nakamura O, *et al.* Comparison of whole brain radiation therapy and locally limited radiation therapy in the treatment of solitary brain metastases from non-small cell lung cancer. *Neurol Med Chir (Tokyo)* 1996;36:364–369.
11. Cull A, Gregor A, Hopwood P, *et al.* Neurological and cognitive impairment in long-term survivors of small cell lung cancer. *Eur J Cancer* 1994;30A:1067–1074.
12. Regine WF, Scott C, Murray K, *et al.* Neurocognitive outcome in brain metastases patients treated with accelerated-fractionation vs. accelerated-hyperfractionated radiotherapy: An analysis from Radiation Therapy Oncology Group Study 91-04. *Int J Radiat Oncol Biol Phys* 2001;51:711–717.
13. Li J, Bentzen SM, Renschler M, *et al.* Regression after whole-brain radiation therapy for brain metastases correlates with survival and improved neurocognitive function. *J Clin Oncol* 2007;25:1260–1266.
14. Folstein MF, Folstein SE, McHugh PR. "Mini-Mental State": A practical method for grading the cognitive state of patients for the clinician. *J Psychiatr Res* 1975;12:189–198.
15. Sundstrom JT, Minn H, Lertola KK, *et al.* Prognosis of patients treated for intracranial metastases with whole-brain irradiation. *Ann Med* 1998;30:296–299.
16. Nagata K, Basugi N, Fukushima T, *et al.* Quantification of brain atrophy [Japanese]. *Brain Nerve* 1985;37:255–262.
17. Taylor BV, Buckner JC, Cascino TL, *et al.* Effects of radiation and chemotherapy on cognitive function in patients with high-grade glioma. *J Clin Oncol* 1998;16:2195–2201.
18. Brown PD, Buckner JC, O'Fallon JR, *et al.* Effects of radiotherapy on cognitive function in patients with low-grade glioma measured by the Folstein Mini-Mental State Examination. *J Clin Oncol* 2003;21:2519–2524.
19. Kleinberg L, Wallner K, Malkin MG. Good performance status of long-term disease-free survivors of intracranial gliomas. *Int J Radiat Oncol Biol Phys* 1993;26:129–133.
20. van Beek AP, van den Bergh ACM, van den Berg LA, *et al.* Radiotherapy is not associated with reduced quality of life and cognitive function in patients treated for nonfunctioning pituitary adenoma. *Int J Radiat Oncol Biol Phys* 2007;68:986–991.
21. Tsuruda JS, Kortman KE, Bradley WG, *et al.* Radiation effects on cerebral white matter: MR evaluation. *AJNR Am J Neuroradiol* 1987;8:431–437.
22. Nieder C, Leicht A, Motaref B, *et al.* Late radiation toxicity after whole brain radiotherapy: The influence of antiepileptic drugs. *Am J Clin Oncol* 1997;22:573–579.
23. Meyers CA, Wefel JS. The use of the Mini-Mental State Examination to assess cognitive functioning in cancer trials: No ifs, ands, buts, or sensitivity. *J Clin Oncol* 2003;21: 3557–3558.
24. Aoyama H, Tago M, Kato N, *et al.* Neurocognitive function of patients with brain metastases who received either whole brain radiotherapy plus stereotactic radiosurgery or radiosurgery alone. *Int J Radiat Oncol Biol Phys* 2007;68:1388–1395.
25. Withers HR. Biologic basis for altered fractionation schemes. *Cancer* 1985;55:2086–2095.
26. Johnson BE, Becker B, Goff WB, *et al.* Neurologic, neuropsychologic, and computed cranial tomography scan abnormalities in 2- to 10-year survivors of small-cell lung cancer. *J Clin Oncol* 1985;3:1659–1667.
27. Lee JS, Umsawasdi T, Lee YY, *et al.* Neurotoxicity in long-term survivors of small cell lung cancer. *Int J Radiat Oncol Biol Phys* 1986;12:313–321.
28. Chak LY, Zatz LM, Wasserstein P, *et al.* Neurologic dysfunction in patients treated for small cell carcinoma of the lung: A clinical and radiological study. *Int J Radiat Oncol Biol Phys* 1986;12:385–389.
29. Poettgen C, Eberhardt W, Grannass A, *et al.* Prophylactic cranial irradiation in operable stage IIIA non-small-cell lung cancer treated with neoadjuvant chemoradiotherapy: Results from a German multicenter randomized trial. *J Clin Oncol* 2007;25: 4987–4992.
30. Murray KJ, Scott C, Zachariah B, *et al.* Importance of the Mini-Mental Status Examination in the treatment of patients with brain metastases: A report from the Radiation Therapy Oncology Group protocol 91-04. *Int J Radiat Oncol Biol Phys* 2000;48:59–64.

IOP PUBLISHING PHYSICS IN MEDICINE AND BIOLOGY

Phys. Med. Biol. **54** (2009) 665–677 doi:10.1088/0031-9155/54/3/013

Computerized method for estimation of the location of a lung tumor on EPID cine images without implanted markers in stereotactic body radiotherapy

H Arimura[1], Y Egashira[2], Y Shioyama[3], K Nakamura[4], S Yoshidome[5], S Anai[5], S Nomoto[3], H Honda[3], F Toyofuku[1], Y Higashida[1], Y Onizuka[1] and H Terashima[1]

[1] Department of Health Sciences, Faculty of Medical Sciences, Kyushu University, 3-1-1, Maidashi, Higashi-ku, Fukuoka 812-8582, Japan
[2] Department of Health Sciences, School of Medicine, Kyushu University, 3-1-1, Maidashi, Higashi-ku, Fukuoka 812-8582, Japan
[3] Department of Clinical Radiology, Graduate School of Medical Sciences, Kyushu University, 3-1-1, Maidashi, Higashi-ku, Fukuoka 812-8582, Japan
[4] Department of Radiology, Faculty of Medicine, Fukuoka University, 8-19-1, Nanakuma, Jyonan-ku, Fukuoka 814-0180, Japan
[5] Division of Radiology, Department of Medical Technology, Kyushu University Hospital, Fukuoka 812-8582, Japan

E-mail: arimura@shs.kyushu-u.ac.jp

Received 5 August 2008, in final form 1 November 2008
Published 9 January 2009
Online at stacks.iop.org/PMB/54/665

Abstract

The purpose of this study was to develop a computerized method for estimation of the location of a lung tumor in cine images on an electronic portal imaging device (EPID) without implanted markers during stereotactic body radiotherapy (SBRT). Each tumor region was segmented in the first EPID cine image, i.e., reference portal image, based on a multiple-gray level thresholding technique and a region growing technique, and then the image including the tumor region was cropped as a 'tumor template' image. The tumor location was determined as the position in which the tumor template image took the maximum cross-correlation value within each consecutive portal image, which was acquired in cine mode on the EPID in treatment. EPID images with 512 × 384 pixels (pixel size: 0.56 mm) were acquired at a sampling rate of 0.5 frame s^{-1} by using energies of 4, 6 or 10 MV on linear accelerators. We applied our proposed method to EPID cine images (226 frames) of 12 clinical cases (ages: 51–83, mean: 72) with a non-small cell lung cancer. As a result, the average location error between tumor points obtained by our method and the manual method was 1.47 ± 0.60 mm. This preliminary study suggests that our method based on the tumor template matching technique might be feasible for tracking the location of a lung tumor without implanted markers in SBRT.

0031-9155/09/030665+13$30.00

1. Introduction

In stereotactic body radiotherapy (SBRT), high dose per fraction is delivered to small tumors and early metastases in lesser fractions. However, it could be possible that enough high doses would not be delivered to a target in a body such as a lung due to respiratory motion (Suh *et al* 2004, Vedam *et al* 2005). Therefore, International Commission on Radiation Units and Measurements (ICRU 1999) Report 62 recommends that the internal margin (IM) should be added outside the clinical target volume (CTV) while taking into account uncertainties in size, shape, locations of the CTV, etc. The sufficient IM to tolerate respiratory motion can be determined, for example, by a slow scan computed tomography (CT) or four-dimensional (4D) CT in each radiotherapy treatment planning (Ford *et al* 2003, Rietzel *et al* 2006, Slotman *et al* 2006, Keall *et al* 2006, Shekhar *et al* 2007, Seco *et al* 2008). However, it is very important to monitor the location of a tumor in cine images by using an electronic portal imaging device (EPID) during SBRT because it has been unclear whether the IM is appropriate for displacements of a tumor due to respiratory motion.

Several methods for monitoring the location of a lung tumor have been developed with or without implanted markers (Keall *et al* 2006, 2004, Shirato *et al* 2000a, 2000b, Shimizu *et al* 2001, Meyer *et al* 2006, Berbeco *et al* 2007). Shirato *et al.* developed a system which was capable of tracking the three-dimensional (3D) position of a metallic marker in the body in real time by means of four sets of diagnostic x-ray imaging equipment (Shirato *et al* 2000a, 2000b, Shimizu *et al* 2001). The system significantly improved the accuracy of irradiation of targets in motion at the expense of an acceptable amount of diagnostic x-ray exposure. Keall *et al* (2004) developed an EPID-based marker-tracking system that can be used for real-time tumor targeting, or 4D radiotherapy. Their study showed that the EPID-based system was feasible for 4D radiotherapy. Meyer *et al* (2006) investigated different algorithms with regard to their suitability to detect and track a moving object in TV camera-based portal images of a phantom without implanted markers. As a result, the best geometric tracking was obtained with the mean of the sum of squared differences. Berbeco *et al* (2007) developed an image-guided method for treatment verification and adaptation during SBRT by using implanted radio-opaque markers. Their clinical experience with the tool indicated that the cine EPID verification modality is a useful tool for tumor localization while the treatment beam is on. Our motivation for this study is a clinical need of software for (1) investigating whether the IM is appropriate for a moving tumor due to respiration, and (2) tracking the moving tumor in real time without implanted markers, because a majority of researchers have used markers implanted adjacent to a tumor, which are invasive approaches for patients. Therefore, our goal of this study was to develop a computerized method for estimation of the location of a lung tumor in EPID cine images during treatment without implanted markers in SBRT.

2. Materials and methods

Figure 1 shows an overall algorithm for estimation of the location of the lung tumor on EPID cine images, which was based on a template matching technique with cross-correlation coefficient (hereafter referred as cross-correlation value). Details of the proposed method are described in this section.

2.1. Determination of an irradiation field image by an automated thresholding technique

The irradiation field region was cropped from an original EPID cine image by analyzing the histogram of the original EPID image (Arimura *et al* 2007). Figure 2 shows the illustration

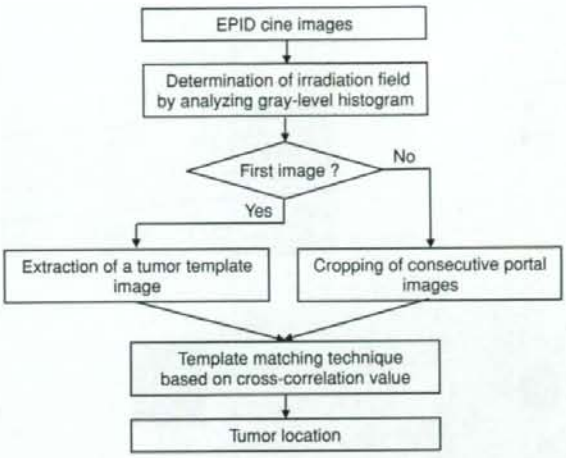

Figure 1. Overall algorithm for estimation of the location of the lung tumor on EPID cine images.

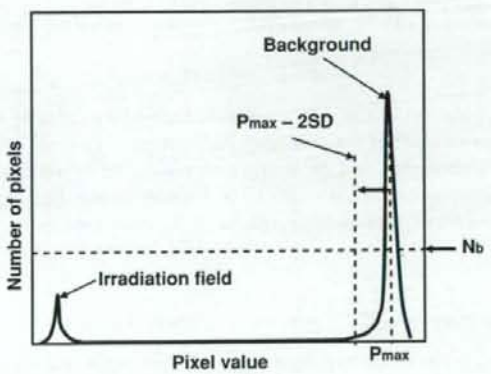

Figure 2. Illustration of a typical histogram in the EPID image, which has small and large peaks corresponding to an irradiation field region and a background (non-irradiation field), respectively.

of a typical histogram in the EPID image, which has small and large peaks corresponding to an irradiation field region and a background (non-irradiation field), respectively. The large peak of the background usually has more than a certain number of pixels, Nb, in the EPID image as shown in figure 2. For extracting the irradiation field region, the maximum pixel value corresponding to the large peak and the standard deviation (SD) were calculated only for a part of the histogram with more than the threshold number of pixels, Nb, which was constant for all cases. Finally, the irradiation field region was determined by binarizing the original EPID image using the maximum pixel value minus twice the SD as shown in figure 2. Figures 3(a) and (b) show an original EPID image and segmented irradiation field region, respectively. Note that the threshold number of pixels, Nb, was empirically determined so that the irradiation fields can be well segmented for all cases, as shown in figure 3(b), where Nb

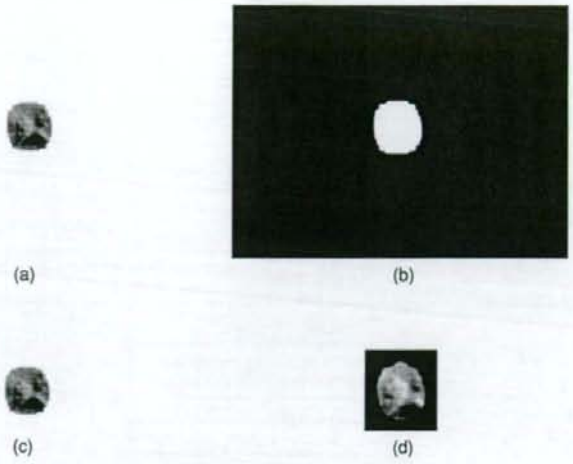

Figure 3. Illustration of (a) an original EPID image, (b) segmented irradiation field region, (c) a rectangular area fitted with the irradiation field region, indicated by dotted lines and (d) cropped image assigned pixel values outside the irradiation field region zero and smoothed by a Gaussian filter, which correspond to the reference portal image or consecutive portal image.

was set as 800. A rectangular area fitted with the irradiation field indicated by a dotted line, as shown in figure 3(c), was cropped as the irradiation field image. The pixel values outside the irradiation field were assigned zero, and the area corresponding to 'set-up margin' defined as 5 mm was eroded by a morphological filter with a 3×3 square kernel. Finally, the irradiation field image was smoothed by a Gaussian filter and one of the irradiation field images is shown in figure 3(d).

2.2. *Extraction of a tumor region and a tumor template image from a reference portal image*

A tumor region was extracted from the first irradiation field image, i.e., reference portal image, by using a multiple-gray level thresholding technique (Arimura *et al* 2004), which is described in the next paragraph, and a region growing technique, and then the cropped image including the tumor region was used as a 'tumor template' image. A Gaussian function was used for the stable production of a tumor template, because it could be easy to segment the tumor region by weighting each pixel value in the reference portal image, where noise and pixel value fluctuations are possible, with the Gaussian function. Since we assume that the tumor would be located at around the centroid of the irradiation field region in the reference portal image, the center of the Gaussian function was put at the centroid of the irradiation field region. The Gaussian-weighted image $I_G(x, y)$ was obtained by the following equation:

$$I_G(x, y) = F(x, y)\left\{-\frac{(x - x_0)^2 + (y - y_0)^2}{2\sigma^2}\right\}, \tag{1}$$

where x and y are the coordinates in the images, x_0 and y_0 were the coordinates of the centroid of the irradiation field region in the reference portal image and σ is the standard deviation of the Gaussian function. The standard deviation was empirically determined so that all tumor

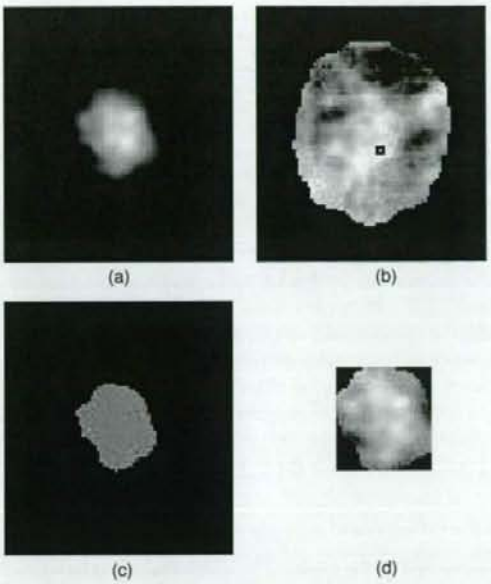

Figure 4. Illustration of (a) a reference portal image multiplied by a 2D Gaussian function, (b) an original reference portal image with a candidate point indicated by an open circle, which was determined by the multiple gray-level thresholding technique, (c) a tumor region segmented by the region growing technique and (d) a tumor template image produced by the proposed method.

regions can be well segmented. In this study, the standard deviation was set as 6.5 mm. Figure 4(a) shows an example of the reference portal image multiplied by the Gaussian filter.

The candidate location of a tumor was identified, as shown in figure 4(b), in the reference portal image by means of the multiple-gray level thresholding technique (Arimura *et al* 2004), which is one of methods for detecting local maximum points in an image in terms of a pixel value by using multiple binary images produced by the corresponding threshold levels. Each threshold level was determined according to a certain specific percentage of the area under the pixel-value histogram in the image. The beginning, ending and increment percentages used for the multiple-gray level thresholding technique were empirically determined so that the local maximum points of all tumor regions can be detected for all cases. The beginning and ending percentages determine the highest and lowest levels, respectively, in terms of the local maximum point, and the increment value determines the resolution of finding local maximum points. The local maximum point was considered as the candidate location of a tumor in this step. In this study, the specific percentages of 1% and 28% were selected as the beginning and ending percentage threshold levels, respectively, with an increment of 1%.

For extracting a tumor region, the region growing started at the candidate location of a tumor determined by the multiple gray-level thresholing technique. A tumor region in the reference portal image was automatically segmented by monitoring two image features, i.e. normalized effective diameter and contrast of the grown region, while a threshold value was changed from the maximum pixel value in the tumor region to 10% of the maximum value, with an increment of 1%. The normalized effective diameter was defined as an effective

diameter, which is a diameter of a circle with the same area as that of the tumor, divided by a longer side length of the reference portal image. The contrast was defined by the following equation:

$$\text{Contrast} = \frac{H_p - L_p}{H_p}, \tag{2}$$

where H_p is the mean pixel value in nine neighbors including a pixel with the maximum pixel value within the tumor region, and L_p is the mean pixel value in the outer region (i.e. narrow band region) of a tumor region. The outer region was considered as a portion of the background of the target, which was empirically determined by dilation of the tumor region so that enough area can be obtained as the background, but the dilated region cannot go over the IF region. In this study, 2.2 mm narrow band-width was set as the outer region. The tumor region was determined if the normalized effective diameter exceeded 0.4 or the contrast exceeded 0.8. This condition was empirically determined so that all tumor regions can be well segmented. Figure 4(c) shows a tumor region obtained by the region growing technique and the morphological dilation operation. The tumor template image, as shown in figure 4(d), was obtained by cropping a rectangular area from the reference portal image fitted with the tumor region and by assigning pixel values outside the tumor region zero.

2.3. Estimation of a tumor location based on a template matching technique

The tumor location was estimated as the position in which the target template image took the maximum cross-correlation value within the consecutive portal image. The coordinate system in the reference portal image was used for the template matching technique. For performing the template matching between the tumor template image $T(x, y)$ and the consecutive portal image $C(x, y)$, the cross-correlation coefficient R was calculated, within the irradiation field as shown in figure 3(b), based on the following equation (Arimura *et al* 2002):

$$R = \frac{1}{N} \sum_{x=0}^{X-1} \sum_{y=0}^{Y-1} \frac{(T(x, y) - \bar{T})(C(x, y) - \bar{C})}{tc}, \tag{3}$$

where x and y are the coordinates in the image, $T(x, y)$ is the pixel value at (x, y) in the tumor template image, $C(x, y)$ is the pixel value at (x, y) in the consecutive portal image, $\bar{T}$ and t are the mean and the standard deviation of the pixel values within the tumor template image $T(x, y)$, respectively, $\bar{C}$ and c are the mean and the standard deviation of the pixel values within the consecutive portal image $C(x, y)$, respectively, and X and Y are the numbers of pixels in x and y widths of the template image, respectively, N is the number of pixels within the irradiation field. The correlation value ranges from -1.0 to 1.0. The template matching was performed for finding a rough tumor location with the maximum cross-correlation value between the tumor template image and the consecutive portal image, by shifting the position of the tumor template image within the irradiation field of the consecutive portal image. Finally, the tumor location was determined by the centroid of the tumor region in the tumor template image, which was put on the consecutive portal image at the pixel with the maximum cross-correlation value.

2.4. Test cases

Twelve cases (age: 51–83 years old, mean: 72) with a non-small cell lung cancer who received a lung stereotactic radiotherapy were selected for this study under the protocol approved by an institutional review board in Kyushu University Hospital. Portal images of these cases

Table 1. Case characteristics for 12 cases used for this study.

Case number	Age (years)	Gender	Tumor location	Effective diameter (mm)	Number of frames
1	77	M	RL	24	16
2	68	M	RL	15	17
3	51	F	RU	20	21
4	81	F	LM	35	7
5	69	F	LM	22	36
6	56	M	RL	15	20
7	80	F	RM	20	17
8	75	F	RM	30	15
9	83	F	LU	27	18
10	71	M	LM	20	18
11	73	M	RU	40	19
12	85	M	LM	20	22
Mean	72	–	–	24	19
SD	10	–	–	8	7

were acquired in cine mode (sampling rate: 0.5 frame s^{-1}) by using an EPID (AS-500, Varian Medical System, Palo Alto, USA) with energies of 4, 6 or 10 MV on linear accelerators (Clinac 21EX, Varian Medical System, Palo Alto, USA). The number of all frames (reference portal images and consecutive portal images) in 12 cases was 226, and the number of all consecutive portal images was 214. Each EPID image consisted of 512 × 384 pixels with a pixel size of 0.56 mm and a gray level scale of 16 bits. The source tumor distance (STD) and the source detector distance (SDD) were 100 cm and 140 cm, respectively. The case characteristics of test cases are shown in table 1. A total dose of 48 Gy was delivered for all patients in four fractions in 1 week. Lung tumors in various locations, i.e. the upper lobe ($n = 3$), middle lobe ($n = 6$) or lower lobe ($n = 3$), were chosen for this study because the displacements of tumor motion depend on the location in a lung due to respiratory motion. The effective diameter d was measured from the clinical target volume (CTV) by using the following equation:

$$d = 2\sqrt[3]{\frac{3V_{\mathrm{CTV}}}{4\pi}} \tag{4}$$

where V_{CTV} is the CTV determined by a radiation oncologist on a treatment planning system (Eclipse, Valian Medical System, Palo Alto, USA).

2.5. *Performance evaluation of our proposed method*

For performance evaluation of the proposed method, we calculated the following two values: (1) the location error, i.e., the Euclidean distance from the 'tumor' point to the candidate point and (2) the overlap measure between the target candidate regions obtained by the manual method and our automated segmentation method. The tumor 'truth' point was defined as the centroid of a tumor region determined manually by a radiation oncologist and a medical physicist, and the tumor region was determined manually by them by using image processing software (Image J, National Institute of Health).

The overlap measure was obtained by the following equation, which denotes the degree of coincidence between the target candidate region C (as shown by a white line in figure 6)

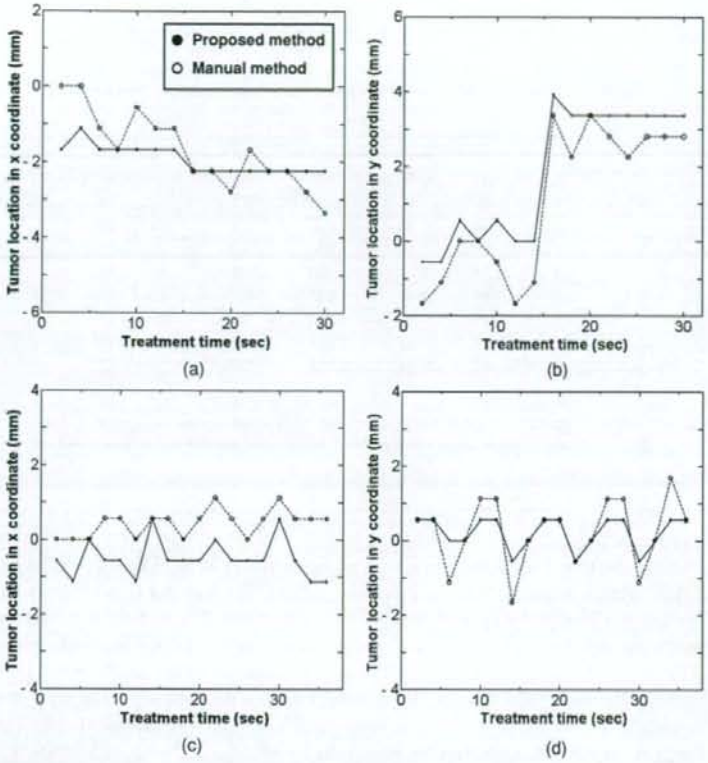

Figure 5. Relative locations of tumors in the x (left–right direction) and y (inferior–superior direction) coordinates for two clinical cases obtained by our proposed method and the manual method: (a) and (b) case 1, and (c) and (d) case 11 in table 1. Solid and open circles indicate target locations obtained by our method and a manual method, respectively.

obtained by our method and the tumor 'truth' region T (as shown by a black line in figure 6) by the manual method:

$$\text{Overlap measure } (\%) = \frac{n(T \cap C)}{n(T \cup C)} \times 100, \tag{5}$$

where T was the tumor region manually determined by a oncologist and a medical physicist, C was the tumor candidate region that automatically determined by using our method, $n(T \cup C)$ is the number of logical OR regions between T and C and $n(T \cap C)$ is the number of logical AND regions between T and C.

3. Results

Figure 5 shows the relative locations of tumors in the x (left–right direction) and y (inferior–superior direction) coordinates for two clinical cases (cases 1 and 11 in table 1) obtained by our proposed method and the manual method. The relative locations were determined based on 'tumor' points in the reference portal images determined by the manual method. Although

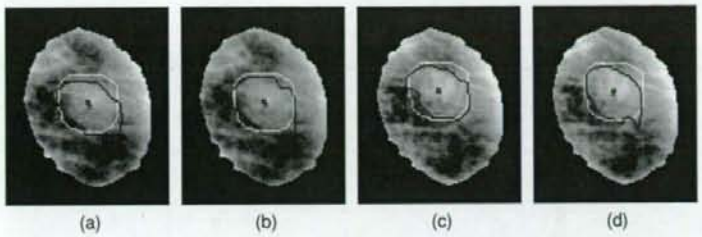

Figure 6. Results of segmentation of a tumor in consecutive portal images in frames 7–10 of case 11 at treatment times of 12, 14, 16 and 18 s. The black line indicates the 'tumor' region determined by the manual method, and the white line indicates the tumor template. Marks of 'x' and 'square' show the tumor locations determined by the manual and our methods, respectively.

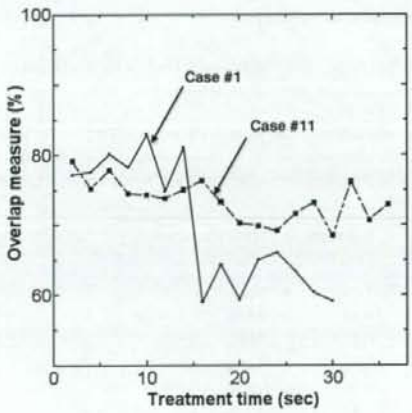

Figure 7. Overlap measures of cases 1 (solid circle, solid line) and 11 (solid square, dot-dashed line) for treatment time.

the tumor location for case 1 in the y coordinate rapidly changed at a treatment time of 16 s as shown in figure 5(b), the tumor location was tracked by our method with an average location error of 1.03 mm. Also, our method traced the tumor location for case 11, which moved periodically as shown in figure 5(d), with an average location error of 1.12 mm. Figures 6(a) to (d) show the results of segmentation of a tumor in consecutive portal images in frames 7–10 of case 1 at treatment times of 12, 14, 16 and 18 s, respectively. Despite an abrupt change at 16 s as shown in figure 5(b), each tumor region in each frame indicated by a black line was well tracked by the tumor template indicated by a white line as shown in figures 6(b) and (c). The tumor region of case 1 was well segmented with an average overlap measure of 69.9% for all frames. Figures 7 and 8 show the overlap measures and location errors, respectively, of cases 1 and 11 for treatment time, respectively. The overlap measure denotes the degree of the coincidence between the tumor regions obtained by the manual and an automated segmentation method, and the location error was defined as the Euclidean distance from the tumor 'truth' point to the candidate point detected by our method. As shown in figure 7, the overlap measure varied with treatment time, and the overlap measure for case 1 dropped down

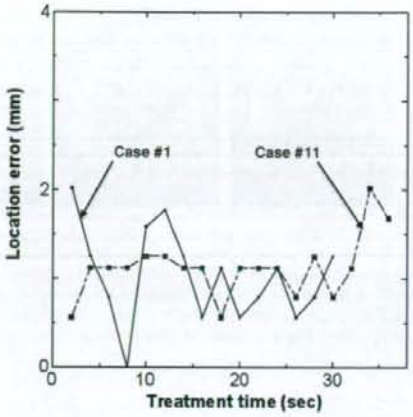

Figure 8. Location errors of cases 1 (solid circle, solid line) and 11 (solid square, dot-dashed line) for treatment time.

Table 2. Performance evaluation of our proposed method for 12 cases, based on the overlap measure (equation (5)), the location error, i.e. Euclidean distance from the true tumor model point to the candidate point, and the maximum cross-correlation value between a tumor template and consecutive portal images.

Case number	Overlap measure (%)	Location error (mm)	Maximum cross-correlation coefficient
1	69.9	1.03	0.883
2	68.0	0.89	0.845
3	68.9	0.86	0.852
4	75.1	1.78	0.806
5	54.9	0.58	0.897
6	73.5	1.48	0.935
7	78.5	2.53	0.905
8	75.5	2.25	0.810
9	68.4	2.02	0.894
10	77.4	1.56	0.919
11	73.4	1.12	0.861
12	78.7	1.49	0.897
Mean	71.9	1.47	0.875
SD	6.6	0.60	0.041

from larger than 80% to smaller than 60% after a treatment time of 15 s. Nevertheless, as shown in figure 8, the location errors were smaller than or equal to 2.0 mm. Table 2 shows the performance evaluation of our proposed method for 12 cases. As a result, the average overlap measure was 71.9 ± 6.6% for 12 cases, and the average location error was 1.47 ± 0.60 mm.

4. Discussion

In summary, the location errors for 79% (168 frames) of 214 frames in 12 cases were smaller than 2.0 mm, which would be required as the minimum error for the standard SBRT, and

those for 94% of all frames were smaller than 3.0 mm. However, we should employ a larger database including a non-small cell cancer with various shapes, locations and sizes in the next step. On the other hand, the overlap measures for 38% (82 frames) of all frames were lower than 70% because most of target regions segmented by the region growing technique were partially overestimated compared with the 'tumor' regions determined by the manual method due to blurred boundaries of the tumors. Since the candidate tumor points were determined based on the centroid of segmented tumor regions extracted by the region growing technique, we should improve our segmentation method based on the region growing technique or other techniques.

Shirato *et al* (2000b) developed a real-time tumor-tracking system with implanted markers using four sets of diagnostic x-ray television systems, and demonstrated that the geometric accuracy of the tumor-tracking system was better than 1.5 mm for moving targets in phantom experiments. Keall *et al* (2004) developed an EPID-based marker-tracking system, and reported that the location errors for implanted markers in dynamic phantom images and the static phantom images are 0.4 mm in EPID. Meyer *et al* (2006) performed a phantom simulation for tracking moving objects, and mentioned that the overall error ranged from 0.15 to 12.6 mm when tracking an object in phantom simulations. Tang *et al* (2007) proposed a marker tracking system that can track multiple markers simultaneously, and reported that tracking errors for fiducial markers in two patients were from 0.6 to 2.3 mm based on an anterior-posterior fluoroscopic video and from 0.2 to 0.4 mm based on a lateral fluoroscopic video for superior-inferior directions. On the other hand, in our study, we have proposed a computerized method for estimation of the location of a lung tumor region without implanted markers. As a result, the average location error between tumor center points obtained by our method and the manual method was 1.47 ± 0.60 mm for 12 patients. In addition, our proposed method estimated each tumor region in each frame of EPID cine images, where the degree of coincidence between the target candidate region obtained by our method and the tumor truth region was $71.9 \pm 6.6\%$ for 12 patients on average. If our software let users know the tumor region within the irradiation field, the users could verify whether the IM would be appropriate for the tumor.

In our method, we assumed that the tumor would be located at around the centroid of the irradiation field region in the first frame, i.e., reference portal image. On that assumption, the tumor template image is produced in the reference portal image for each patient. However, if the tumor moved out of the centroid of the irradiation field region due to the respiration motion or setup errors in the reference portal image, the tumor template image would include some errors. In fact, the location errors for three cases (cases 7–9) were larger than 2.0 mm, which might show the relatively low accuracy for these cases. The reason can be explained as follows. Figure 9 shows the illustration of the tumor 'truth' region and its centroid indicated by a black line and '*x*', respectively, and of the tumor template region and its centroid indicated by a white line and 'square', respectively, for case 7. The tumor truth region indicated by a black line is displaced out of the centroid of the tumor template region indicated by a white line. In this case, the distance between the centroids of the tumor truth region and tumor template region was 2.24 mm. Such a displacement, as shown in figure 9, leads to larger location error, and the problem occurred for the other two cases. Therefore, we should improve the production method of the tumor template in future work.

A report of AAPM Task group 76 (Keall *et al* 2006) recommended that a real-time tumor tracking method should preferably provide three-dimensional (3D) coordinates of the tumor, although two-dimensional (2D) motion in the plane perpendicular to the beam direction such as our proposed method is also acceptable. The EPID images acquired by oblique beams at least two images or more should be needed for measuring the 3D coordinates of the tumor

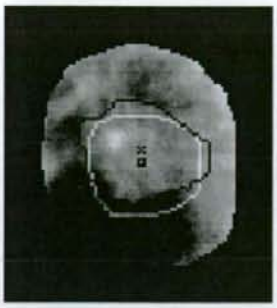

Figure 9. Illustration of a tumor 'truth' region and centroid indicated by a black line and 'x', respectively, and of the tumor template region and centroid indicated by a white line and 'square', respectively, for case 7.

locations. In future work, we will attempt to develop a method for the 3D coordinates of the tumor based on the oblique acquisitions of the EPID images.

We believe that the reproducibility of the results obtained by the proposed method is important for many researchers. Therefore, in this paper, we described all empirical procedures for determination of several parameters, e.g., a parameter for segmentation of the irradiation field, the standard deviation of a Gaussian function in equation (1), parameters for the multiple-gray level thresholding technique and a parameter used for the outer region of contrast in equation (2). However, all parameters are associated with the image quality of the EPID cine images, which depend on manufacturers and institutions. Therefore, if researchers apply our proposed method to their EPID cine images, they should adjust each parameter according to the procedures presented in this paper.

The final goal of our study is to develop a real-time tumor tracking method during treatment without implanted markers in SBRT. The frame acquisition time was 2 s/frame, because the frame rate was 0.5 frame s^{-1}, which was determined by the specification of the EPID used in this study. On the other hand, the processing time was about 1.8 s/frame on average for determination of a tumor region and location by using 2.4 GHz central processing unit (CPU) and 4 GB memory. The processing time might be acceptable for the current system used in this study, but could be unacceptable for the latest EPID system. Although the template matching technique took most of the calculation time, the faster CPUs could process the technique rapider than our result. Nevertheless, the report of Task group 76 (Keall *et al* 2006) recommended that the total time delay of the real-time tracking system should be kept as short as possible and not more than 0.5 s because the breathing irregularity makes it difficult to predict more than 0.5 s with sufficient accuracy. Therefore, we should improve the proposed method in terms of the calculation time for clinical use.

5. Conclusions

We have proposed a computerized method for estimation of the lung tumor location in EPID cine images during treatment without implanted markers in SBRT. As a result, the average location error between tumor center points obtained by our method and the manual method was 1.47 $\pm$ 0.60 mm. The location errors for 79% of all frames (214 frames) in 12 cases were smaller than 2.0 mm, and those for 94% of all frames were smaller than 3.0 mm. This

preliminary study suggests that our proposed method based on the tumor template matching technique might be feasible for monitoring a tumor location without implanted markers in SBRT.

Acknowledgments

The authors are grateful to Mr Kouhei Hisano, Dr Junji Morishita and Dr Masafumi Ohki for useful discussion, and R Chartrand, MA, for improving our manuscript.

References

Arimura H, Anai S, Yoshidome S, Nakamura K, Shioyama Y, Nomoto S, Honda H, Onizuka Y and Terashima H 2007 Computerized method for measurement of displacement vectors of target positions on EPID cine images in stereotactic radiotherapy *SPIE Proc.* **6512** 65121U1-8

Arimura H, Katsuragawa S, Li Q, Ishida T and Doi K 2002 Development of a computerized method for identifying the posteroanterior and lateral views of chest radiographs by use of a template matching technique *Med. Phys.* **29** 1556–61

Arimura H, Katsuragawa S, Suzuki K, Li F, Shiraishi J and Doi K 2004 Computerized scheme for automated detection of lung nodules in low-dose CT images for lung cancer screening *Acad. Radiol.* **11** 617–29

Berbeco R I, Hacker F, Ionascu D and Mamon H J 2007 Clinical feasibility of using an EPID cine mode for image-guided verification of stereotactic body radiotherapy *Int. J. Radiat. Oncol. Biol. Phys.* **69** 258–66

Ford E C, Mageras G S, Yorke E and Ling C C 2003 Respiration-correlated spiral CT: a method of measuring respiratory induced anatomic motion for radiation treatment planning *Med. Phys.* **30** 88–97

International Commission on Radiation Units and Measurements (ICRU) 1999 Prescribing, Recording and Reporting Photon Beam Therapy (Supplement to ICRU Report 50) *Report 62* (Bethesda: ICRU)

Keall P J *et al* 2006 The management of respiratory motion in radiation oncology report of AAPM Task Group 76 *Med. Phys.* **33** 3874–900

Keall P J, Todor A D, Vedam S S, Bartee C L, Siebers J V, Kini V R and Mohan R 2004 On the use of EPID-based implanted marker tracking for 4D radiotherapy *Med. Phys.* **31** 3492–9

Meyer J, Richter A, Baier K, Wilbert J, Guckenberger M and Flentje M 2006 Tracking moving objects with megavoltage portal imaging: a feasibility study *Med. Phys.* **33** 1275–80

Rietzel E, Lui A K, Doppke K P, Wolfgong J A, Chen A B, Chen G T and Choi N C 2006 Design of 4D treatment planning target volumes *Int. J. Radiat. Oncol. Biol. Phys.* **66** 287–95

Seco J, Sharp G C, Wu Z, Gierga D, Buettner F and Paganetti H 2008 Dosimetric impact of motion in free-breathing and gated lung radiotherapy: a 4D Monte Carlo study of intrafraction and interfraction effects *Med. Phys.* **35** 356–66

Shekhar R, Lei P, Castro-Pareja C R, Plishker W L and D'Souza W D 2007 Automatic segmentation of phase-correlated CT scans through nonrigid image registration using geometrically regularized free-form deformation *Med. Phys.* **34** 3054–66

Shimizu S, Shirato H, Ogura S, Dosaka H, Kitamura K, Nishioka T, Kagei K, Nishimura M and Miyasaka K 2001 Detection of lung tumor movement in real-time tumor-tracking radiotherapy *Int. J. Radiat. Oncol. Biol. Phys.* **51** 304–10

Shirato H *et al* 2000a Four-dimensional treatment planning and fluoroscopic real-time tumor tracking radiotherapy for moving tumor *Int. J. Radiat. Oncol. Biol. Phys.* **48** 435–42

Shirato H *et al* 2000b Physical aspects of a real-time tumor-tracking system for gated radiotherapy *Int. J. Radiat. Oncol. Biol. Phys.* **48** 1187–95

Slotman B J, Lagerwaard F J and Senan S 2006 4D imaging for target definition in stereotactic radiotherapy for lung cancer *Acta Oncol* **45** 966–72

Suh Y, Yi B, Ahn S, Kim J, Lee S, Shin S, Shin S and Choi E 2004 Aperture maneuver with compelled breath (AMC) for moving tumors: a feasibility study with a moving phantom *Med. Phys.* **31** 760–6

Tang X, Sharp G C and Jiang S B 2007 Fluoroscopic tracking of multiple implanted fiducial markers using multiple object tracking *Phys. Med. Biol.* **52** 4081–98

Vedam S, Docef A, Fix M, Murphy M and Keall P J 2005 Dosimetric impact of geometric errors due to respiratory motion prediction on dynamic multileaf collimator-based four-dimensional radiation delivery *Med. Phys.* **32** 1607–20

Jpn J Clin Oncol 2008;38(4)275–280
doi:10.1093/jjco/hyn014

Variation of Clinical Target Volume Definition among Japanese Radiation Oncologists in External Beam Radiotherapy for Prostate Cancer

Katsumasa Nakamura[1], Yoshiyuki Shioyama[2], Sunao Tokumaru[3], Nobuyuki Hayashi[4], Natsuo Oya[5], Yoshiyuki Hiraki[6], Kazuo Kusuhara[7], Takafumi Toita[8], Hiroaki Suefuji[9], Naofumi Hayabuchi[9], Hiromi Terashima[10], Masaoki Makino[11] and Kenichi Jingu[12]

[1]Department of Radiology, School of Medicine, Fukuoka University, Fukuoka, [2]Department of Clinical Radiology, Graduate School of Medical Sciences, Kyushu University, Fukuoka, [3]Department of Radiology, Faculty of Medicine, Saga University, Saga, [4]Department of Radiology, Nagasaki University School of Medicine, Nagasaki, [5]Department of Radiation Oncology, Kumamoto University Hospital, Kumamoto, [6]Department of Radiology, Kagoshima University School of Medicine, Kagoshima, [7]Department of Radiology, Miyazaki Medical College, Miyazaki, [8]Department of Radiology, Graduate School of Medical Science, University of the Ryukyus, Okinawa, [9]Department of Radiology, Kurume University School of Medicine, Kurume, Fukuoka, [10]Department of Health Sciences, School of Medicine, Kyushu University, Fukuoka, [11]Department of Radiology, National Hospital Organization Kagoshima Medical Center, Kagoshima and [12]Division of Radiation Oncology, St. Mary's Hospital, Fukuoka, Japan

Received November 29, 2007; accepted February 7, 2008; published online March 12, 2008

Background: We investigated the interobserver variation in the prostate target volume and the trend toward the use of diagnostic computed tomography (CT) or magnetic resonance (MR) images for treatment planning.
Methods: Twenty-five radiation oncologists were asked to draw the external contour of the prostate on CT images (0.3 cm spacing) of a patient with localized prostate cancer. They also answered a questionnaire regarding the use of diagnostic CT or MR images for the contouring.
Results: Of the 25 physicians, 28% rarely or never referred to the diagnostic CT images. In contrast, the physicians tended to refer to the MR images more frequently. Approximately 50% of the physicians believed in the usefulness of contrast-enhanced images for the delineation of the prostate. As for the variation of the prostate contouring, the median craniocaudal prostate length was 36 mm (range, 21–54 mm), and the median prostate volume was 43.5 cm^3 (range, 23.8–98.3 cm^3). The interobserver variability was not significant in the duration as a radiation oncologist, the board certification status as radiation oncologists, and the number of treatment plans developed for prostate cancer during the last 1 year.
Conclusion: A wide variety of the definitions of the prostate was found among Japanese radiation oncologists.

Key words: radiation oncology – urologic-RadOncol – radiology-CT/MRI

INTRODUCTION

Three-dimensional conformal radiotherapy (3DCRT) is used in many institutions for the treatment of localized prostate cancer in Japan (1,2). As 3DCRT can decrease the incidence of normal tissue toxicity, the dose delivered to the tumor can be higher than the dose delivered with conventional techniques for the same complication rate. Dose-escalation studies in patients with prostate cancer have been reported to improve the biochemical relapse-free survival rates (3,4). The radiation doses employed in Japanese institutions have also been increasing (1,2,5). To achieve a good treatment result, ensuring adequate coverage of the target area remains necessary.

Currently, one of the most important challenges for 3DCRT is the accurate delineation of tumor and target volumes (6). Several studies have shown marked

For reprints and all correspondence: Katsumasa Nakamura, Department of Radiology, School of Medicine, Fukuoka University, 7-45-1 Nanakuma, Jonan-ku, Fukuoka, 814-0180 Japan. E-mail: nakam@fukuoka-u.ac.jp

interobserver variability in target volume definition for prostate cancer (7–9). However, there have been few reports on this type of study among Japanese radiation oncologists.

This study aimed to investigate the interobserver variation in the prostate target volume among Japanese radiation oncologists. In addition, we evaluated the trend toward the use of diagnostic computed tomography (CT) or magnetic resonance (MR) images for treatment planning.

MATERIALS AND METHODS

Twenty-five radiation oncologists, who attended the 18th Annual Meeting for Radiation Oncologists in Kyushu, were enrolled in this study. The characteristics of the physicians were as follows: the median period of their career as a radiation oncologist was 8 years (range, 1–36 years) and 12 physicians (48%) were board-certificated radiation oncologists. All but one physician had experience with CT-based 3DCRT. The numbers of treatment plans for prostate cancer developed during the last 1 year were: 0–9, eight physicians (32%); 10–19, eight physicians (32%); 20–39, six physicians (24%); and >40, three physicians (12%).

The sample questionnaire for the contouring of the prostate is included in the Appendix. Briefly, it consisted of two sections: (1) questions regarding the use of diagnostic CT or MR images for the contouring; and (2) the sample CT images of a patient with localized prostate cancer for the delineation of the prostate.

The CT images were obtained using a Mx8000 (Philips Medical Systems, Andover, MA, USA). The CT data set (0.3 cm spacing) was from a patient with localized prostate cancer, who was treated by 3DCRT. This patient was considered to be typical, with an average prostate shape and size.

For the delineation of the prostate, 25 physicians were asked to draw its outline as the clinical target volume (CTV) directly on a high-quality hard copy (Appendix). The craniocaudal prostate length was calculated from the number of slices contoured multiplied by the slice thickness. The volume of the typical CTV outline of the prostate was calculated using three-dimensional treatment planning software Eclipse (Varian, Palo Alto, CA, USA). For the calculation of the prostate volume, the contours of the prostate were cut away from the hard copy, measured on a high-precision electrical balance (Sartorius BP211D, Goettingen, Germany), and compared with the weight of the typical CTV volume.

The Student's *t*-test was used to compare means. A P value <0.05 was considered to indicate a statistically significant difference.

RESULTS

The trend toward the use of diagnostic CT and MR images for the contouring is shown in Fig. 1. Of all physicians, seven physicians (28%) rarely or never referred to the diagnostic CT images. In contrast, the physicians tended to refer to the MR images more frequently. As for the contrast-enhanced CT or MR images, approximately 50% of the physicians believed in the usefulness of contrast materials for the delineation of the prostate (Fig. 2).

The interobserver variation of the CTV delineation is shown in Fig. 3. The median craniocaudal prostate length and CTV volume were 36 mm (range, 21–54 mm) and 43.5 cm^3 (range, 23.8–98.3 cm^3), respectively. Although the board-certificated radiation oncologists tend to contour the prostate with smaller variability, the interobserver variation was not significant with regard to the duration as a radiation oncologist, the board certification status as radiation oncologists, and the numbers of treatment plans developed for prostate cancer during the last 1 year (Figs. 4–6).

DISCUSSION

The interobserver differences in the target volume definition for prostate cancer have been investigated. Livsey et al. (8)

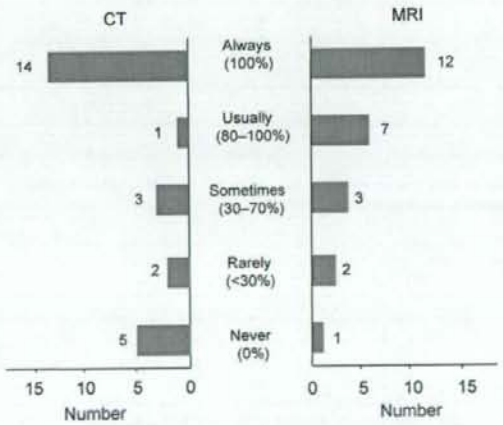

Figure 1. The use of diagnostic images for the delineation of the prostate. Computed tomography (CT), magnetic resonance imaging (MRI).

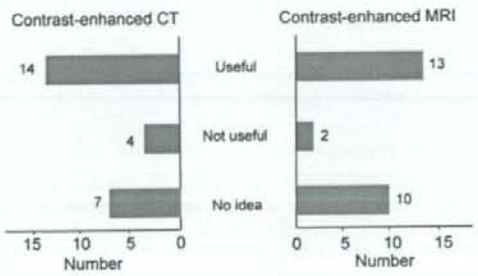

Figure 2. The opinions of radiation oncologists about the usefulness of contrast-enhanced images for the prostate delineation.